



## Self-weakening in lithiated graphene electrodes

Hui Yang<sup>a</sup>, Xu Huang<sup>a</sup>, Wentao Liang<sup>a</sup>, Adri C.T. van Duin<sup>b,\*</sup>, Muralikrishna Raju<sup>b</sup>, Sulin Zhang<sup>a,\*</sup>

<sup>a</sup> Department of Engineering Science and Mechanics, Pennsylvania State University, University Park, PA 16802, USA

<sup>b</sup> Department of Mechanical and Nuclear Engineering, Pennsylvania State University, University Park, PA 16802, USA

### ARTICLE INFO

#### Article history:

Received 30 October 2012

In final form 25 January 2013

Available online 1 February 2013

### ABSTRACT

We present a molecular dynamics study of the fracture mechanisms of lithiated graphene. Our modeling results reveal that lithium diffusion toward the crack tip is both energetically and kinetically favored owing to the crack-tip stress gradient. The stress-driven lithium diffusion results in lithium aggregation around the crack tip, chemically weakening the crack-tip bond and at the same time causing stress relaxation. Our simulations show that the chemical weakening effect is the dominant factor, which manifests a self-weakening mechanism in lithiated graphene. The atomistic understanding of the degradation mechanism provides guidance for the lifetime extension in the design of graphene-based electrodes.

© 2013 Elsevier B.V. All rights reserved.

### 1. Introduction

Graphene and carbon nanotubes (CNTs) not only possess outstanding mechanical properties and electronic characteristics, but also hold significant promise as anode materials in lithium (Li) ion batteries (LIBs) [1–7]. Due to their high electrical conductivity, they have been used as conducting additives to other active materials in electrodes [8,9]. Because of their unique geometries, CNTs and layered graphene possess enhanced energy storage capacities [10–13] as compared to the conventional Li-graphite anodes. Owing to their great flexibility and high fracture strength, they are also expected to exhibit longer cycle life [14,15] than conventional carbonaceous anodes.

Recent experimental studies evidenced that CNTs undergo mechanical degradation upon electrochemical cycling, and showed that CNTs were broken into smaller pieces after up to a few hundred or thousand cycles [16–18]. More recently, Liu et al. reported that lithiation drastically embrittles multi-walled carbon nanotubes (MWCNTs) [18], but not layered graphene [19,20]. It was argued that the different mechanical responses stem from in the geometrical constraints of MWCNT and layered graphene. For MWCNTs, the inter-wall Li intercalation causes ~6% hoop strain [18]. In contrast, graphene in layered geometry can freely bend into the third dimension [19], thereby suppressing the buildup of high in-plane stretching energy that would cause fracture. Despite the obvious difference in the lithiated multi-layered graphene and MWCNTs, the embrittlement of MWCNTs remains to be understood from a mechanics perspective, given the fact that a pristine CNT can sustain an in-plane strain up to 20% or even larger [21].

During lithiation of an MWCNT, Li intercalation into the graphene layers generates tensile stress in the hoop direction. The intercalated Li can be regarded as adatoms of the graphene layers, which also chemically weakens the graphene. Previous molecular orbital theory calculations showed that the presence of a single Li weakens the pristine graphene by ~30% [18]. Owing to these weakening factors, small cracks may nucleate, either homogeneously, or from preexisting atomic vacancies. The nucleation processes are beyond the scope of the present Letter. Instead, we herein carry out molecular dynamics (MD) simulations to elucidate the lithiation-induced failure mechanisms of monolayer graphene, with a focus on the effect of Li on the propagation of a preexisting crack in monolayer graphene. While the focus of the present Letter is lithiated monolayer graphene, the modeling results can be straightforwardly extended to CNTs by taking into account of the curvature effects. We show that the stress gradient at the crack tip drives Li adatoms migrating toward the crack tip. The aggregation of Li at the crack tip lead to two consequences: weakening the crack-tip bond due to the local chemical Li–C reaction and causes stress relaxation of the high Li-concentration region. Through MD simulations, we identify that the chemical weakening effect is the dominant factor on the crack propagation in graphene. We further point out that the stress-diffusion coupling effect and the crack-tip Li-aggregation induced fracture behavior are universal in the degradation of electrodes. Our studies offer a fundamental guidance to the cycle life extension of CNT- and graphene-based anodes in LIBs, and shed light on the failure mechanisms of other important anode materials such as Si.

### 2. Methodology

In our MD simulations, the interatomic interactions are modeled by the ReaxFF reactive force field. The ReaxFF combines a

\* Corresponding authors.

E-mail addresses: [acv13@enr.psu.edu](mailto:acv13@enr.psu.edu) (A.C.T. van Duin), [suz10@psu.edu](mailto:suz10@psu.edu) (S. Zhang).

bond-distance/bond order relationship with a geometry-dependent charge calculation, and provides a highly transferable method, applicable to covalent, metallic and ionic materials and their interfaces [22–24]. The ReaxFF generally fits not only thermodynamic properties at equilibrium states, but also kinetic properties including reaction barriers, both from first-principles based simulations. The ReaxFF has been adequately shown to provide an accurate account of the chemo-mechanical behavior of the hydrocarbon systems, while capable of treating thousands of atoms [25–27]. We have tested the accuracy of the ReaxFF after introducing Li into the hydrocarbon system. For instance, the migration barrier from one hollow site (the center of the hexagons) to another on a monolayer graphene calculated by the ReaxFF differs only 3% from the density functional theory (DFT) calculations [28,29]. The functional form of the ReaxFF and parameters are given in Supplementary.

To simulate Li-mediated crack propagation in graphene, we adopt a size-reduced model (1910 carbon atoms in total) consisting of a small circular-shaped domain cut around a crack tip [30,31], as shown in Figure 1. In classical fracture mechanics, the asymptotic stress profile  $\sigma_{ij}$  for a plane-stress condition in the region sufficiently close to a crack tip can be written as:

$$\sigma_{ij} = \frac{K_1^{\text{app}}}{\sqrt{2\pi r}} H_{ij}(\theta); \quad (1)$$

where  $r$  and  $\theta$  are the polar coordinates with the origin  $O$  sitting at the crack tip,  $H$  is the known angular dependent function,  $i$  and  $j$  are the two Cartesian coordinate indices. Note that the asymptotic stress at the crack tip is dominated by a single loading parameter, i.e., the applied stress intensity factor (SIF)  $K_1^{\text{app}}$ , independent of

the geometry of the specimen. Such a domain at the crack tip is known as the  $K$ -dominant zone. In our simulation model, the domain size is chosen such that its outer boundary falls in the  $K$ -dominant zone. Such a small system can effectively model a long crack that extends self-similarly under applied  $K$  load with considerably reduced computational cost.

To generate the asymptotic stress profile described in Eq. (1) in the atomic system around a crack tip, we impose the crack-tip displacement on the atoms consistent with the asymptotic stress field. To begin with, the pristine graphene system is dynamically relaxed at 10 K free of any constraints using the Berendsen thermostat. Starting from the relaxed system, atoms about 3 Å from the outer boundary (red dots in Figure 1) are held fixed, while the remainder of atoms is set free. All the atoms in the system are then displaced according to the displacement field of the crack-tip asymptotic solution dictated by the applied SIF, with the origin  $O$  taking as the center of the circular graphene:

$$\begin{aligned} u_x &= \frac{K_1^{\text{app}}}{2\mu} \frac{r}{2\pi} (\kappa - \cos \theta) \cos(\theta/2) \\ u_y &= \frac{K_1^{\text{app}}}{2\mu} \frac{r}{2\pi} (\kappa - \cos \theta) \sin(\theta/2) \end{aligned}; \quad (2)$$

where  $\mu$  is the shear modulus of the lattice,  $\kappa = (3 - \nu)/(1 + \nu)$ , and  $\nu = 0.4$  is the Poisson's ratio directly obtained from MD simulations. Due to the applied  $r^{1/2}$ -dependent displacement, a crack appears with the crack tip at  $O$ . The stress distribution of the strained circular graphene can be obtained by evaluating the Virial stress at all the atomic sites, followed by the interpolation over the entire graphene surface [32]. Our simulations demonstrate that the Virial stress distribution agrees very well with the continuum asymptotic

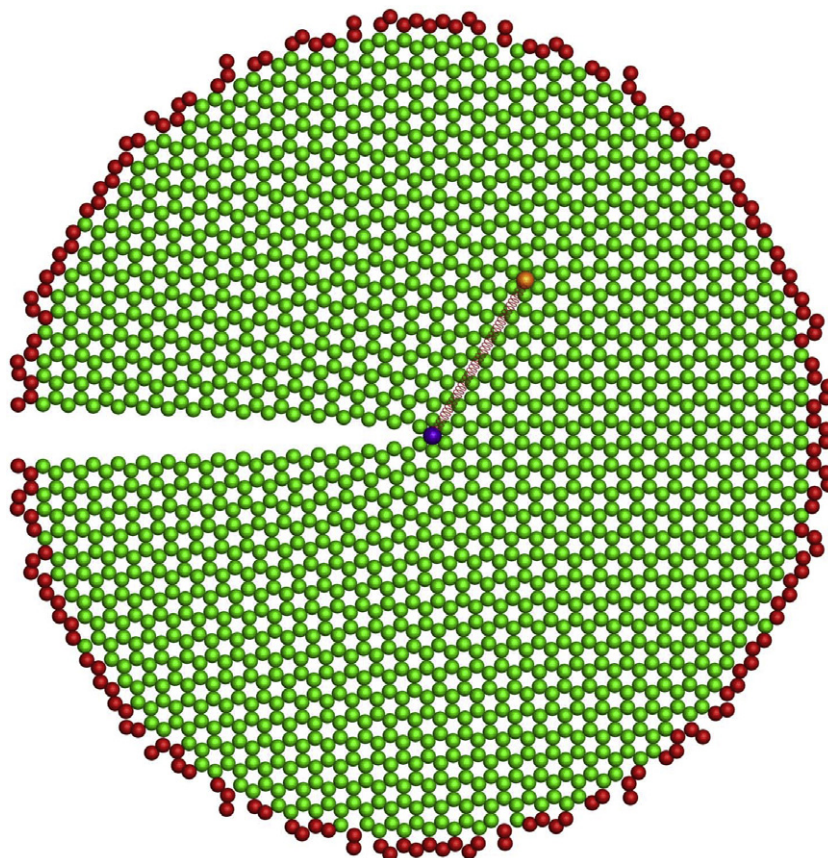


**Figure 1.** The size-reduced simulation model for analyzing the lithiation induced fracture in graphene. The circular domain can be loaded by prescribing the displacement field in Eq. (2), where the red dots represent the carbon atoms that are fixed, while the green dots are free carbon atoms. In determining the mobility of Li adatom, a dummy atom at the crack tip (purple) is connected to the Li adatom (gold) at the far with a virtual spring of high stiffness. (For interpretation of the references to colour in this figure legend, the reader is referred to the web version of this article.)

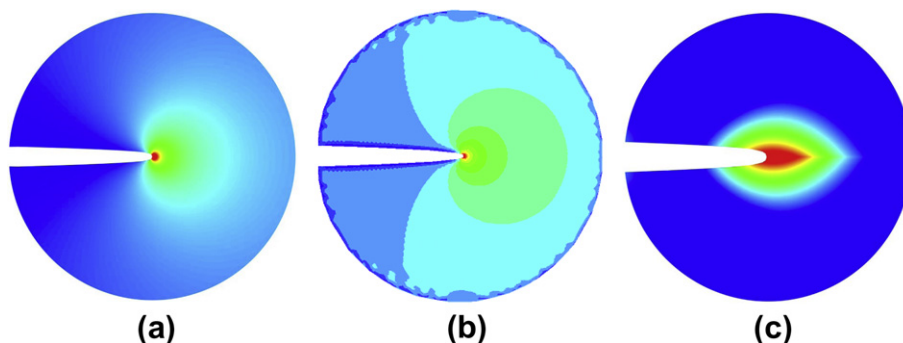


**Figure 2.** Stress-mediated stability of Li adatom. (a) The pressure profile at the crack tip obtained from continuum fracture mechanics ( $P \propto \cos(\theta=2)$ ). (b) Virial stress profile at the crack tip; (c) the stability map. From green to red colors the stability of the Li adatom increases. The high-stability domain at the crack tip is inconsistent with the high-pressure contour in (a) and (b), suggesting that shear stress and possibly the free crack edges play additional roles in the stability of the Li adatom. (For interpretation of the references to colour in this figure legend, the reader is referred to the web version of this article.)

stress field (only hydrostatic stress is plotted as an example) we intended to mimic, as shown in Figure 2a, demonstrating the validity of the model.

### 3. Results and discussion

#### 3.1. Li stability on a cracked graphene

Upon successfully setting the stress field at the crack tip, we next determine the stability and mobility of an adatom Li under the stressed environment of the crack tip. We place an adatom Li at different hollow sites and compute the binding energy by imposing the  $K$ -dominant displacement field at prescribed  $K$  values. The system is then dynamically relaxed at low temperature (10 K) with and without the Li adatom. For a graphene consisting of  $n$  carbon atoms, the binding of a Li adatom can be expressed by



where  $\text{C}_n$  denotes the pure graphene, the product on the right side of the arrow is the graphene with a Li adatom. The energy difference  $\Delta E = E(\text{LiC}_6 + \text{C}_{n-6}) - E(\text{Li}) - E(\text{C}_n)$  gives rise to the binding (formation) energy of the Li adatom. Interpolation of the binding energy over the entire simulation model gives rise to a stability map, as shown in Figure 2c. The map clearly shows that the closer the Li adatom to the crack tip, the higher the thermodynamic stability of the system. We noticed that the Li stability map is not fully con-

sistent with the high-pressure concentration profile at the crack tip. The inconsistency suggests that the shear stress and the free edges (crack surface) may play a certain role in the Li stability.

#### 3.2. Migration pathways and kinetic barriers of Li on a cracked graphene

We further calculate the migration barriers of Li adatoms from the far field to the crack tip in order to evaluate the Li mobility under the stress gradient at the crack tip. We choose the bridge site of the crack-tip bond as a fixed dummy point because of its higher stability than the crack-tip hollow site. A virtual harmonic spring is then generated to link the dummy point and Li adatom at the far field on the graphene (Figure 1). The equilibrium length of the spring at the beginning is set to be the initial distance between the dummy point and the Li adatom. The equilibrium length of the spring is then decreased incrementally, followed by system energy minimization at each step until the Li adatom moves to the dummy point. The stiffness of the spring is set to be very high such that at each step the bond length is highly constrained to the equilibrium length of the spring, while the bond can freely rotate in the 3D space, thereby enabling the exploration of the minimum energy path. Due to the high stiffness, the energy stored in the spring at each step is negligibly small. The energy landscape along the minimum energy path can be then determined from the total system energy and the spring length (i.e., reaction coordinate). Figure 3

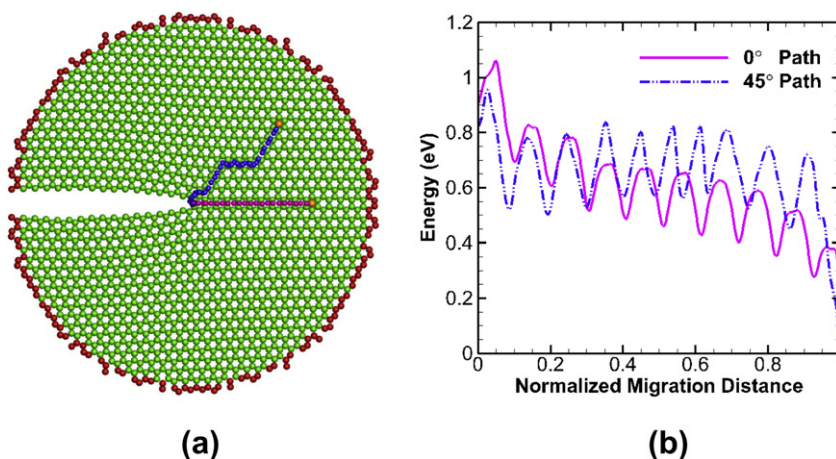


**Figure 3.** The mobility of the Li adatom. (a) The migration paths (minimum energy paths) for a Li adatom initially placed along  $\theta = 0$  (path indicated by a sequence of blue dots) and  $\theta = 45$  (path indicated by a sequence of pink dots) migrating toward the crack-tip hollow site. (b) The migration energy landscapes corresponding to the migration paths. (For interpretation of the references to colour in this figure legend, the reader is referred to the web version of this article.)

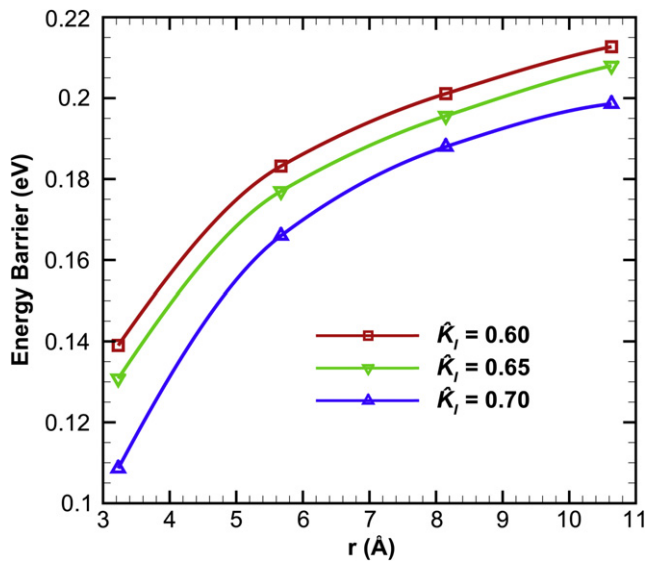


**Figure 4.** Load dependent migration barrier of the Li adatom ( $\theta = 0$ ). As the applied load (stress intensity factor  $K_I = K_I = 2\mu$ ), the migration barrier decreases.

shows the migration paths and barrier of the Li adatom along two directions:  $\theta = 0$  and  $45^\circ$ .

Similar to the Li stability, the mobility of the Li adatom increases as it gets closer to the crack tip, manifested by the increasingly reduced migration barrier. Figure 3 a depicts the migration paths of the adatom Li initially placed at three representative positions on the graphene ( $\theta = 0^\circ$ ,  $45^\circ$ , and  $60^\circ$ ). For the Li adatom placed along the direction of  $\theta = 0^\circ$  and  $60^\circ$  (not shown), the adatom Li migrates along a straight path, i.e., the  $[1-100]$  direction. However, for the Li adatom placed at the direction of  $\theta = 45^\circ$ , the adatom Li adopts a non-straight migration path: rather than

migration along  $\theta = 45^\circ$  direction to reach the crack-tip hollow site, the Li adatom take two  $\theta = 60^\circ$  migration path segments, connected by a horizontal migration path. Figure 3b plots the corresponding migration energy landscapes for the adatom Li placed. In general, the migration barrier decreases as the adatom moves toward the crack tip. Our calculations further show that the migration barrier also decreases with the increase of the applied stress intensity factors, as seen in Figure 4.

The above analysis shows that Li diffusion to the crack tip is both thermodynamically and kinetically favored, driven by the stress gradient around the crack tip. The stress-driven Li diffusion therefore causes the concentration of Li around the crack tip, i.e., the Li concentration gradient is in the opposite direction of the stress gradient:  $\nabla c \propto \nabla P$ , where  $P = -(\sigma_{rr} + \sigma_{\theta\theta})/3$  is the pressure. The Li distribution has two possible consequences on the fracture of the graphene: (a) the Li adatom at the crack tip may significantly weaken the crack-tip bond, giving rise to a reduced bond strength, and therefore a reduced fracture strength; and (b) concentrating Li at the crack tip may cause local stress relaxation [33]. Both the consequences modulate the onset condition of the crack propagation.

### 3.3. Chemical weakening and crack-tip stress relaxation due to Li aggregation

We next assess how aggregation of Li at the crack tip modifies the fracture behavior of the graphene. We conceive that the Li adatoms at and around the crack tip may reduce the crack-tip C-C bond strength and at the same time disturb the stress distribution. To explore the coupled effects, we consider four configurations with different Li concentrations around the crack tip, forming a crystal core embedded in an outer pristine graphene shell. Configuration  $X_0$  is simply the pristine circular graphene sheet without any Li adatoms (not shown); configuration  $X_1$  is the graphene sheet with a single adatom placing at the hollow site of the crack tip (Figure 5a); configuration  $X_2$  is the graphene sheet with  $\text{LiC}_6$

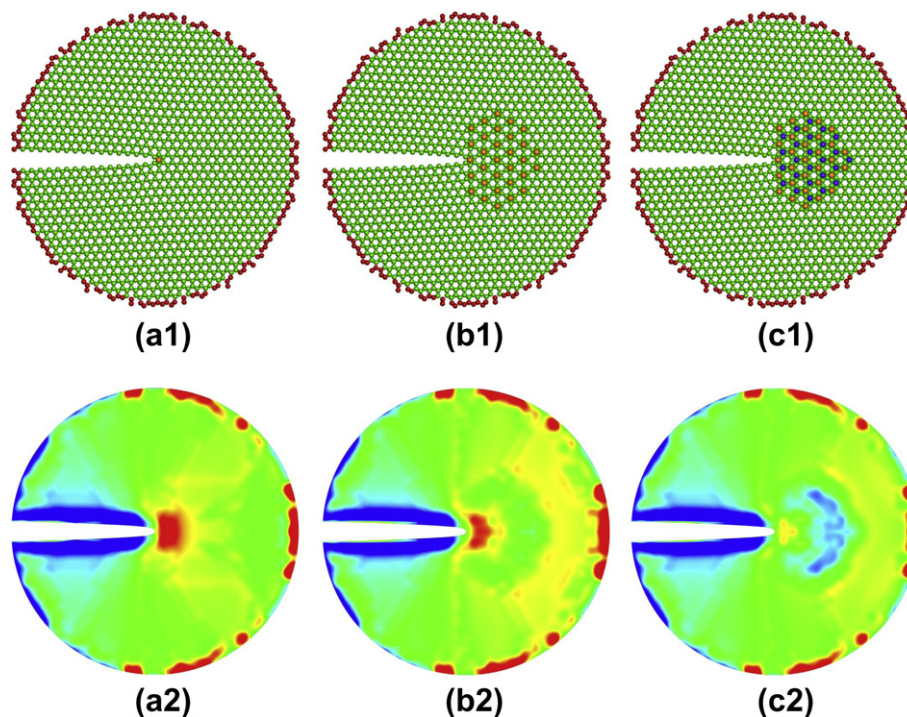


**Figure 5.** Chemical weakening and stress relaxation due to Li aggregation to the crack tip, demonstrated by the profiles of Virial stress for different Li concentration at the crack tip. Top row from left to right: Configuration  $X_1$  to  $X_3$ . Li adatoms are around the crack tip. For  $X_3$ , the Li adatoms on the different sides of graphene are marked by different colors. Bottom row from left to right: hydrostatic stress of the configurations corresponding to the top row.

around the crack tip and all the Li are placed on one side of the graphene (Figure 5b); and configuration  $X_3$  with  $LiC_3$  around the crack tip (Figure 5c) [34,35]. The difference in the fracture strength between  $X_1$  and  $X_0$  gives rise to the chemical weakening effect of the single adatom at the crack-tip; while the difference between  $X_1$  and  $X_2$ , and  $X_3$  to the effect of Li aggregation on the fracture strength. It should be noted that it has raised heated debates as to the maximal concentration of Li on a graphene surface [36,37]. Here, we do not intend to fuel the debates, but focus on the chemo-mechanical consequence of concentrated Li at the crack tip.

We calculate the fracture loads at which the first C–C bond at the crack tip breaks for the four configurations by numerically determining the critical stress intensity factor  $K_I$ . Our systematic simulations showed that the fracture loads are 0.86 for configuration  $X_0$ , 0.75 for configuration  $X_1$ , 0.71 for  $X_2$ , and 0.70 for  $X_3$ . The fracture load for  $X_1$  is significantly lower than that for  $X_0$ , indicating that the strong chemical weakening effect of the Li adatom to the crack-tip C–C bond. With increasing Li concentration at the crack tip, the fracture load decreases, further confirming the weakening effects of the Li adatoms on the graphene surface.

In addition to the chemical weakening effect, concentrating Li adatoms on the crack tip also perturbs the stress around the crack tip [33]. To verify this effect, we calculated the hydrostatic stress on the carbon atoms around the crack tip using the Virial formula for the three cases ( $X_1$ ,  $X_2$ , and  $X_3$ ), as shown in Figure 5(a2–c2). Indeed, the hydrostatic stress is moderately relaxed due to the aggregation of Li adatoms around the crack tip. The stress level suggests the magnitude of the driving force for the crack propagation. Thus, stress relaxation due to the presence of Li adatoms should theoretically lead to an increase of the fracture load [33], opposite to the chemical weakening effect. Our calculated fracture loads, however, decrease with increasing Li concentration. This suggests that the chemical weakening effect overshadows the stress relaxation effect. It should be noted that with increasing Li concentration, the reduction in the fracture load decreases. For example, the fracture loads for  $X_2$  and  $X_3$  are nearly the same. This indicates that the stress relaxation becomes increasing more pronounced with further increased Li concentration. It can be followed that the stress relaxation would become the dominant factor and the fracture loads would increase beyond a critical Li concentration.

#### 4. Conclusions

In conclusion, we have studied the lithiation-induced fracture mechanisms of graphene using MD simulations with the ReaxFF reactive force field. The new ReaxFF can be used for atomistic study of phase transformation, Li diffusion, defect nucleation and growth etc., of a wide range of carbonaceous materials. Our simulations show that the stress gradient around the crack tip drives the Li migration toward the crack tip, leading to the aggregation of Li around the crack tip. The aggregation of Li locally reduces the bond strength on the one hand, and causes stress relaxation at the crack tip on the other. The former reduces the fracture strength, while the latter reduces the fracture driving force (and hence increases the fracture strength). In the case of lithiated graphene, the former factor is dominant. Taking together of the stress-gradient driven Li migration and subsequent reduced fracture strength, lithiated graphene exhibits a self-weakening mechanism that causes the fracture of the graphene.

We wish to point out that the strong coupling between the crack-tip stress gradient and the Li migration, as well as the subsequent weakening/strengthening effects are universal for all the electrodes upon lithiation. Giving Si as an example, the stress-gradient will lead to the concentration Li at the crack-tip. However,

due to the large volume expansion (300%) upon lithiation, the stress relaxation effect may be dominant over the chemical weakening effect [33]. As a result, concentration of Li may arrest propagating crack. Our studies shed lights on the lithiation-induced embrittlement of MWCNTs and pave the way to mitigate the degradation of graphene-based anode materials in LIBs.

#### Acknowledgements

H.Y. and S.L.Z. acknowledge NSF support under grants CMMI-1201058 and CMMI-0900692. A.C.T.v.D. and M.R. acknowledge the support of the Fluid Interface Reactions, Structures and Transport (FIRST) Center, an Energy Frontier Research Center funded by the U.S. Department of Energy, Office of Science, Office of Basic Energy Sciences for the development of the Li/C ReaxFF force field parameters.

#### Appendix A. Supplementary data

Supplementary data associated with this article can be found, in the online version, at <http://dx.doi.org/10.1016/j.cplett.2013.01.048>.

#### References

- [1] L. Dai, D.W. Chang, J.-B. Baek, W. Lu, *Small* 8 (2012) 1130.
- [2] G. Centi, S. Perathoner, *ChemSuschem* 4 (2011) 913.
- [3] M. Pummera, *Energy Environ. Sci.* 4 (2011) 668.
- [4] J.B. Hou, Y.Y. Shao, M.W. Ellis, R.B. Moore, B.L. Yi, *Phys. Chem. Chem. Phys.* 13 (2011) 15384.
- [5] D.A.C. Brownson, D.K. Kampouris, C.E. Banks, *J. Power Sources* 196 (2011) 4873.
- [6] N.A. Kaskhedikar, J. Maier, *Adv. Mater.* 21 (2009) 2664.
- [7] C. de las Casas, W.Z. Li, *J. Power Sources* 208 (2012) 74.
- [8] X.-L. Wang, W.-Q. Han, *ACS Appl. Mater. Interfaces* 2 (2010) 3709.
- [9] B.J. Landi, M.J. Ganter, C.D. Cress, R.A. DiLeo, R.P. Raffaele, *Energy Environ. Sci.* 2 (2009) 638.
- [10] B.J. Landi, C.D. Cress, R.P. Raffaele, *J. Mater. Res.* 25 (2010) 1636.
- [11] M. Liang, L. Zhi, *J. Mater. Chem.* 19 (2009) 5871.
- [12] T. Bhardwaj, A. Antic, B. Pavan, V. Barone, B.D. Fahlman, *J. Am. Chem. Soc.* 132 (2010) 12556.
- [13] Y. Chan, J.M. Hill, *Nanoscale Res. Lett.* 6 (2011) 203.
- [14] J. Chen, A.I. Minett, Y. Liu, C. Lynam, P. Sherrell, C. Wang, G.G. Wallace, *Adv. Mater.* 20 (2008) 566.
- [15] G. Wang, X. Shen, J. Yao, J. Park, *Carbon* 47 (2009) 2049.
- [16] C. Masarapu, V. Subramanian, H. Zhu, B. Wei, *Adv. Funct. Mater.* 19 (2009) 1008.
- [17] V.G. Pol, M.M. Thackeray, *Energy Environ. Sci.* 4 (2011) 1904.
- [18] Y. Liu et al., *ACS Nano* 5 (2011) 7245.
- [19] X.H. Liu et al., *Carbon* 50 (2012) 3836.
- [20] X.H. Liu, Y. Liu, A. Kushima, S. Zhang, T. Zhu, J. Li, J.Y. Huang, *Adv. Energy Mater.* 2 (2012) 722.
- [21] S.L. Mielke et al., *Chem. Phys. Lett.* 390 (2004) 413.
- [22] A.C.T. van Duin, S. Dasgupta, F. Loran, W.A. Goddard, *J. Phys. Chem. A* 105 (2001) 9396.
- [23] S.S. Han, A.C.T. van Duin, W.A. Goddard, H.M. Lee, *J. Phys. Chem. A* 109 (2005) 4575.
- [24] M.F. Russo, A.C.T. van Duin, *Nucl. Instrum. Methods Phys. Res. B* 269 (2011) 1549.
- [25] X. Huang, H. Yang, A.C.T. van Duin, K.J. Hsia, S. Zhang, *Phys. Rev. B* 85 (2012) 195453.
- [26] S.P. Kim, A.C.T. van Duin, V.B. Shenoy, *J. Power Sources* 196 (2011) 8590.
- [27] K. Chenoweth, S. Cheung, A.C.T. van Duin, W.A. Goddard, E.M. Kober, *J. Am. Chem. Soc.* 127 (2005) 7192.
- [28] Y. Kubota, N. Ozawa, H. Nakanishi, H. Kasai, *J. Phys. Soc. Jpn.* 79 (2010) 014601.
- [29] K.T. Chan, J.B. Neaton, M.L. Cohen, *Phys. Rev. B* 77 (2008) 235430.
- [30] S. Zhang, T. Zhu, T. Belytschko, *Phys. Rev. B* 76 (2007) 094114.
- [31] S.S. Terdalkar, S. Huang, H.Y. Yuan, J.J. Rencis, T. Zhu, S.L. Zhang, *Chem. Phys. Lett.* 494 (2010) 218.
- [32] S.L. Zhang, R. Khare, Q. Lu, T. Belytschko, *Int. J. Numer. Methods Eng.* 70 (2007) 913.
- [33] R. Grantab, V.B. Shenoy, *J. Electrochem. Soc.* 159 (2012) A584.
- [34] A.M. Garay-Tapia, A.H. Romero, V. Barone, *J. Chem. Theory Comput.* 8 (2012) 1064.
- [35] X. Fan, W.T. Zheng, J.-L. Kuo, *ACS Appl. Mater. Interfaces* 4 (2012) 2432.
- [36] E. Pollak, B. Geng, K.-J. Jeon, I.T. Lucas, T.J. Richardson, F. Wang, R. Kostecki, *Nano Lett.* 10 (2010) 3386.
- [37] E. Lee, K.A. Persson, *Nano Lett.* 12 (2012) 4624.